Structure sensitivity in the ruthenium nanoparticle catalyzed aqueous-phase Fischer-Tropsch reaction

Catalysis Science & Technology

PAPER

View Article Online
View Journal | View Issue

CrossMark click for updates

Cite this: *Catal. Sci. Technol.*, 2014, 4, 3510

Structure sensitivity in the ruthenium nanoparticle catalyzed aqueous-phase Fischer–Tropsch reaction

Xian-Yang Quek, Robert Pestman, Rutger A. van Santen and Emiel J. M. Hensen*

Received 31st May 2014,
Accepted 27th June 2014

DOI: 10.1039/c4cy00709c

www.rsc.org/catalysis

Low-temperature Fischer–Tropsch reaction data are reported for Ru nanoparticles suspended in the water phase. Their activity and selectivity strongly depends on particle size, when varied between 1 to 5 nm. Small particles display high oxygenates selectivity. The Anderson–Schulz–Flory (ASF) chain-growth probability for oxygenates is significantly lower than that observed for hydrocarbons. The chain growth parameter for hydrocarbon formation is independent of particle size. For oxygenates it is constant only for particles larger than 3 nm. Oxygenate and hydrocarbon formation occur on different sites. The ASF chain-growth probability for oxygenate formation increases with temperature. For very small 1.2 nm particles it shows a maximum as a function of temperature. This unusual temperature dependence is due to relatively slow CO dissociation compared to the rate of C–C bond formation.

1. Introduction

Alternative carbon resources such as biomass, natural gas, and coal are increasingly considered as possible feedstock for the synthesis of liquid transportation fuels and chemicals with the aim to reduce our dependence on crude oil reserves. A versatile and increasingly popular catalytic route is their conversion by steam reforming or gasification into synthesis gas (a mixture of CO and H_2) followed by the Fischer–Tropsch (FT) reaction.[1–5] Co, Fe and Ru are the typical transition metals that catalyze the reaction of synthesis gas into long-chain hydrocarbons.[2–4] The rate of CO dissociation on less reactive transition metals such as Ni is too low and methane is the main product.[6] On metals such as Ir and Pt the rate of CO dissociation is also slow. Rh has intermediate reactivity and shows interesting oxygenate selectivity.[1] Here, we will present low-temperature catalytic performance data of small unsupported Ru nanoparticles, which exhibit high selectivity to long-chain oxygenates next to long-chain hydrocarbons.

Among the various mechanisms proposed to account for the formation of long-chain hydrocarbons,[7] the carbide mechanism has found most support in literature. According to this mechanism, the building blocks for chain growth are CH_x surface intermediates.[7,8] The Fischer–Tropsch reaction then comprises three main surface reaction steps: (i) CO dissociation and formation of CH_x intermediates, (ii) chain growth by CH_x insertion and subsequent hydrogen transfer steps, and (iii) termination to form the final product. On surfaces of low reactivity, CO dissociation may proceed *via* the H-assisted pathway[9,10] instead of direct CO dissociation.[11] For the chain-growth step involving CH_x surface intermediates, different routes have been proposed such as Brady–Pettit alkyl[12] and the Gaube–Maitlis alkelydene/alkenyl[13] mechanisms. There are three different termination steps possible, namely H addition, β-H elimination and CO insertion respectively giving rise to paraffins, olefins and oxygenates.

Within the carbide mechanism, a prerequisite for formation of long-chain products is that the rate of methane formation is low in order to provide sufficient CH_x intermediates to maintain a high rate of chain growth.[7] Also, for production of long-chain products the rate of termination should be relatively low compared to the rate of chain growth. This implies that increased rate of chain-growth termination by CO insertion or hydrogen transfer reactions would decrease the rate of chain growth, and, accordingly, the chain growth probability (α). When oxygenate and hydrocarbon formation is the result of competition for the same growing adsorbed hydrocarbon chain, increased selectivity towards oxygenate formation implies that the intrinsic rate for chain-growth termination to oxygenates is faster than that for chain-growth termination to hydrocarbon. The chain growth probabilities of both products would then be the same. The main alternative proposal to the carbide mechanism for the FT reaction is the one formulated by Pichler and

Schuit Institute of Catalysis, Laboratory of Inorganic Materials Chemistry, Eindhoven University of Technology, P.O. Box 513, 5600 MB Eindhoven, The Netherlands. E-mail: e.j.m.hensen@tue.nl; Fax: +31 40 2455054; Tel: +31 40 2475178

Schulz,[14,15] who postulated that CO inserts into the growing chain followed by C–O dissociation (CO insertion mechanism). Then the rate of CO activation may be slow compared to the rate of chain growth.[7] In this case, high selectivity towards oxygenates reduces chain-growth probability strongly compared to formation of hydrocarbons.

Whereas Fischer–Tropsch catalysis can be considered structure insensitive for relatively large transition metal particles,[16] a strong size dependence has been observed when the particles become smaller than 10 nm.[17–22] Recent gas-phase SSITKA data for hydrocarbon production indicate that with decreasing Ru nanoparticle size the relative fraction of reactive sites decreases without change of the intrinsic activity.[22] For Co particles, there are strong indications that also the intrinsic reactivity of the active centers changes with particle size.[20] The critical particle size below which the CO consumption rate becomes structure sensitive is in the 7–10 nm range for Co[17–20] and 6–10 nm for Ru.[21,22] This structure sensitive behavior has been attributed to the decreasing stability of step-edge sites on the surface of smaller particles. These sites are essential for low-barrier CO dissociation.[7,8] An alternative explanation is that CO or C atoms adsorb too strongly on small particles, thus poisoning part of the catalytic surface.[17–20] Salmeron *et al.* recently suggested that particle size effects in the FT reaction are due to differences in the rate of H_2 dissociation, thus affecting the rate of H-assisted CO dissociation.[23] It is also known that smaller particles produce more methane and have a lower C_{5+} selectivity.[17,22] Apart from particle size, the crystal structure of nanoparticles also affects their catalytic performance. Recent studies indicate that hcp-Co is more active than fcc-Co.[24,25]

Similar to commercial practice, most laboratory studies on the FT reaction are carried out in fixed-bed or slurry-phase reactors. An interesting alternative approach involving FT reaction in the aqueous phase in a batch reactor was recently demonstrated by Xiao *et al.*[26] In this pioneering work, the dominant reaction products were reported to be hydrocarbons. We have recently performed similar experiments focusing on the effect of the reaction temperature.[27] We found that Ru nanoparticle catalysts produce a mixture of long-chain hydrocarbons and oxygenates under these anomalous conditions (water solvent, temperatures below 200 °C). Exceptionally high selectivity towards long-chain aldehydes and alcohols was observed at temperatures below 200 °C.[27] We have proposed that hydrocarbons form on sites with low barrier for CO dissociation, likely involving step-edge sites, whereas oxygenates are thought to form on sites with a higher barrier for CO dissociation. Recently, Wang *et al.* investigated the effect of ionic promoters on the Ru-catalyzed FT reaction and also reported increased oxygenate selectivity.[28]

In this contribution, we report about the effect of Ru nanoparticle size and reaction conditions on the activity and selectivity in aqueous-phase FT. Polyvinylpyrrolidone (PVP) stabilized Ru nanoparticles in the 1 to 6 nm range were prepared and characterized. Bulk and surface characterization of these catalysts by synchrotron XRD-PDF and their overall performance in aqueous phase FTS have been reported before.[29] Here, we expand on this initial study by providing detailed insight into the influence of particle size and reaction temperature on the activity and selectivity in the aqueous-phase FT reaction. The results will be discussed in the frame of the carbide and CO insertion mechanisms.

2. Experimental and computational methods

2.1 Synthesis of materials

Polyvinylpyrrolidone (PVP, M_n = 10 000 g mol^{-1}, Sigma Aldrich) stabilized Ru nanoparticles were synthesized using 1,4-butanediol or H_2 as the reducing agent. Ruthenium(III) chloride hydrate ($RuCl_3{\cdot}nH_2O$, Alfa Aesar) and ruthenium(III) acetylacetonate ($Ru(acac)_3$, Aldrich) were used as Ru precursors. The reduction by 1,4-butanediol was carried out in a similar manner as earlier described for Rh.[29] In a typical synthesis (PVP/Ru molar ratio of 20), 30 mg of $Ru(acac)_3$ and 0.17 g of PVP were dissolved in 2 mL of tetrahydrofuran (THF, Sigma Aldrich) and 3 mL of 1,4-butanediol (Sigma-Aldrich). The mixture was then added to 27 mL of 1,4-butanediol, which was preheated at 225 °C, followed by refluxing in a N_2 atmosphere for 2 h. The resulting black suspension was thoroughly washed with acetone and diethyl ether. After collecting the Ru nanoparticles by centrifugation, they were redispersed in 1.5 mL distilled water. In cases where reduction was carried out in hydrogen, first 40 mg of $RuCl_3{\cdot}xH_2O$ and 0.22 g of PVP were dissolved in 1 mL of distilled water in a 10 mL autoclave. The autoclave was then pressurized with 20 bar H_2 followed by heating to 150 °C for 2 h under vigorous stirring. The resultant black suspension was washed, collected by centrifugation, and redispersed in 3 mL distilled water. Catalysts are denoted by Ru-*x* where *x* stands for the average particle size in nm.

2.2 Characterization

The concentration of the Ru nanoparticles dispersed in water was determined by inductively coupled plasma atomic emission spectroscopy (ICP-AES) analysis performed on a Goffin Meyvis SpectroCirus apparatus. Transmission electron micrographs (TEM) were made with a FEI Tecnai 20 electron microscope equipped with a LaB_6 filament and operating at an acceleration voltage of 200 kV. A small amount of the nanoparticles was mixed with ethanol, dispersed over a carbon-coated Cu grid and finally dried in air. The average particle size and the standard deviation were determined by analyzing at least 150 particles. FTIR spectra of adsorbed CO were collected using a heated attenuated total reflectance (HATR) flow cell from Spectra-Tech ARK with a Si 45° crystal (cutoff at 1500 cm^{-1}) in a Nicolet Protégé 460 FTIR spectrometer equipped with a liquid-nitrogen cooled MCT detector. Prior to the IR measurement, the Ru nanoparticles dispersed in water were re-reduced in an autoclave at 150 °C with

20 bar H_2 for 2 h under vigorous stirring. The Ru particles were then spin-coated onto the Si crystal under N_2 atmosphere. The coated Si crystal was then mounted and sealed in the ATR cell under N_2 atmosphere. The sample was dried by flowing 5 mL min^{-1} of He at 80 °C for 30 min. Subsequently, CO was introduced in the cell at a flow of 2.5 mL min^{-1}. After an isothermal period at 50 °C for 0.5 h, the cell was heated to 150 °C. FTIR spectra were recorded 5 min after reaching 150 °C in absorbance mode at a resolution of 4 cm^{-1}. A total of 32 scans were measured in this way, followed by subtraction of the background spectrum of the Si crystal. X-ray Absorption Spectra (XAS) were recorded in a home-built transmission cell for liquid samples at the Dutch Belgium Beamline (DUBBLE) of the European Synchrotron Radiation Facility (ESRF, Grenoble, France). A droplet of the liquid containing the Ru nanoparticles was placed between Kapton windows. XAS spectra were collected in fluorescence mode at the Ru K-edge with a 9-channel solid-state detector. Energy selection was done by a double crystal Si(111) monochromator. EXAFS analysis was performed with EXCURVE931 on k^3-weighted unfiltered raw data using the curved wave theory. Phase shifts were derived from *ab initio* calculations using Hedin–Lundqvist exchange potentials and Von Barth ground states as implemented in EXCUREVE98. In a typical experiment, 28 μmol of Ru dispersed in 200 μL of H_2O was transferred into the XAS cell. The cells were then transferred to the beamline and the EXAFS spectra were recorded at room temperature.

2.3 Catalytic activity measurements

Prior to reaction, an amount of catalyst (50 μmol Ru) was dispersed in 3 mL of deionized water and re-reduced in a 10 mL stainless steel autoclave at 150 °C with 20 bar H_2 for 2 h under vigorous stirring. After reduction, the autoclave was cooled to room temperature in an ice bath before releasing the pressure. The liquid phase FT reaction was carried out at 30 bar using reaction times between 3 and 24 h. The autoclave was flushed 3 times with CO, before being pressurized with CO followed by H_2 to 30 bar (molar ratio H_2/CO = 2). The autoclave was sealed and the autoclave body was heated to the reaction temperature with a band heater controlled by a temperature controller. The reaction was terminated by immersing the autoclave into an ice bath. The reaction time varied between 3 to 24 h so as to maintain a maximum pressure drop of 10 bar in the reactor. The gas-phase products were analyzed with an Interscience Compact GC system, equipped with an Al_2O_3/KCl column and a flame ionization detector (FID). For analysis, the gas cap was flushed through a 6-way valve allowing injection onto a gas chromatograph. Methane, ethane, ethylene, propane and propylene were analyzed against a standard gas mixture. For analysis of the liquid phase, an extraction was carried out with diethyl ether containing *p*-cymene as an internal standard. The organic phase containing the products was then analyzed with a GC (QP5050, Shimadzu) equipped with a Rxi-5ms capillary column (30 m × 0.25 mm × 0.5 μm) and a flame ionization detector (FID). Identification and quantification of linear alkanes (C_6 to C_{16}), alcohols (C_4 to C_{12}) and aldehydes (C_4 to C_{12}) was established with reference compounds and *p*-cymene as the internal standard. GC response factors for other hydrocarbons (C_{17+}) and oxygenates (C_{13+}) were estimated by extrapolation. The identity of the products was also verified with a GC-MS equipped (GC-MS, QP5050, Shimadzu) with a Rxi-5 ms capillary column.

The rate of the FT reaction (r), turnover frequency (TOF), and selectivity were calculated based on the number of moles of carbon being formed in the products according to the following formula:

$$r = \frac{\text{Total mol C formed in all products}}{\text{Mass of Ru} \times \text{reaction time}} \quad (1)$$

$$\text{TOF} = \frac{\text{Total mol C formed in all products}}{(\text{mol Ru}_{\text{surface atoms}}) \times \text{reaction time}} \quad (2)$$

$$\text{Selectivity to hydrocarbon or oxygenate} = \frac{\sum(\text{mol of C}_n^{\text{HC/oxy}} \times n)}{\text{Total mol C formed as products}} \quad (3)$$

with the mol $Ru_{surface\ atoms}$ = mol Ru × D.

The dispersion (D) was calculated assuming spherical shapes by using the formula given by Scholten *et al.*[30]

$$D = 10^{21} \times \frac{6 \times M \times \rho_{\text{site}}}{d_{\text{p}} \times N_{\text{Av}} \times \rho_{\text{metal}}} \quad (4)$$

with M being the atomic weight of Ru, ρ_{site} the surface density (16.3 Ru atom nm^{-2}), ρ_{metal} the density of metal (12.3 g cm^{-3}), d_p the Ru particle size and N_{Av} the Avogadro's number. Hydrocarbon selectivity includes alkanes and alkenes and oxygenate selectivity aldehydes and alcohols.

3. Results

3.1 Catalyst characterization

Table 1 summarizes the conditions used to synthesize Ru nanoparticles. The reduction method, reduction temperature and the Ru source were varied to control the size of Ru nanoparticles between 1.2 nm to 5.2 nm (Fig. 1). In a standard synthesis using polyol reduction of $RuCl_3$ at 195 °C for 2 h, we obtained on average 2.3 nm Ru particles (Ru-2.3). By using $Ru(acac)_3$ instead of $RuCl_3$ under otherwise similar conditions we obtained larger particles (Ru-3.7). We found that increasing the temperature of reduction of $RuCl_3$ by the polyol was not an effective method to control the Ru particle size. For instance, the average Ru particle size only increased slightly from 2.3 nm to 2.5 nm when the reduction temperature was increased from 195 to 225 °C. In contrast, by polyol reduction of the $Ru(acac)_3$ precursor at different temperatures we were able to obtain nanoparticle catalysts with

Table 1 Synthesis conditions and properties of Ru nanoparticles[a]

Catalyst	Reduction method[b]	T (°C)	Ru source	d_p[c] (nm)	Fraction Ru^0 (%)[d]	c_{Ru}[e] (μmol mL^{-1})
Ru-1.2	H_2	145	$RuCl_3$	1.2 ± 0.4	90	35.6
Ru-2.3	Polyol	195	$RuCl_3$	2.3 ± 0.3	85	35.8
Ru-2.7	Polyol	165	$Ru(acac)_3$	2.7 ± 0.3	—	35.9
Ru-3.4	Polyol	175	$Ru(acac)_3$	3.4 ± 0.5	80	34.1
Ru-3.7	Polyol	195	$Ru(acac)_3$	3.7 ± 0.5	90	33.2
Ru-4.3	Polyol	215	$Ru(acac)_3$	4.3 ± 0.6	—	29.0
Ru-5.2	Polyol	225	$Ru(acac)_3$	5.2 ± 0.8	92	32.6

[a] Ru nanoparticles synthesis parameters: PVP/Ru molar ratio = 20, M_n (PVP) = 10 000, re-dispersed in 1.5 mL H_2O. [b] Polyol: 1,4-butanediol as reducing agent, H_2: 20 bar H_2 as reducing agent. [c] Average particle size and standard deviation determined by TEM analysis. [d] Determined from XANES after second reduction with 20 bar H_2 at 150 °C. [e] Determined from ICP-AES elemental analysis for the synthesized Ru nanoparticles dispersed in 1.5 mL H_2O (theoretical concentration: 50 μmol mL^{-1}).

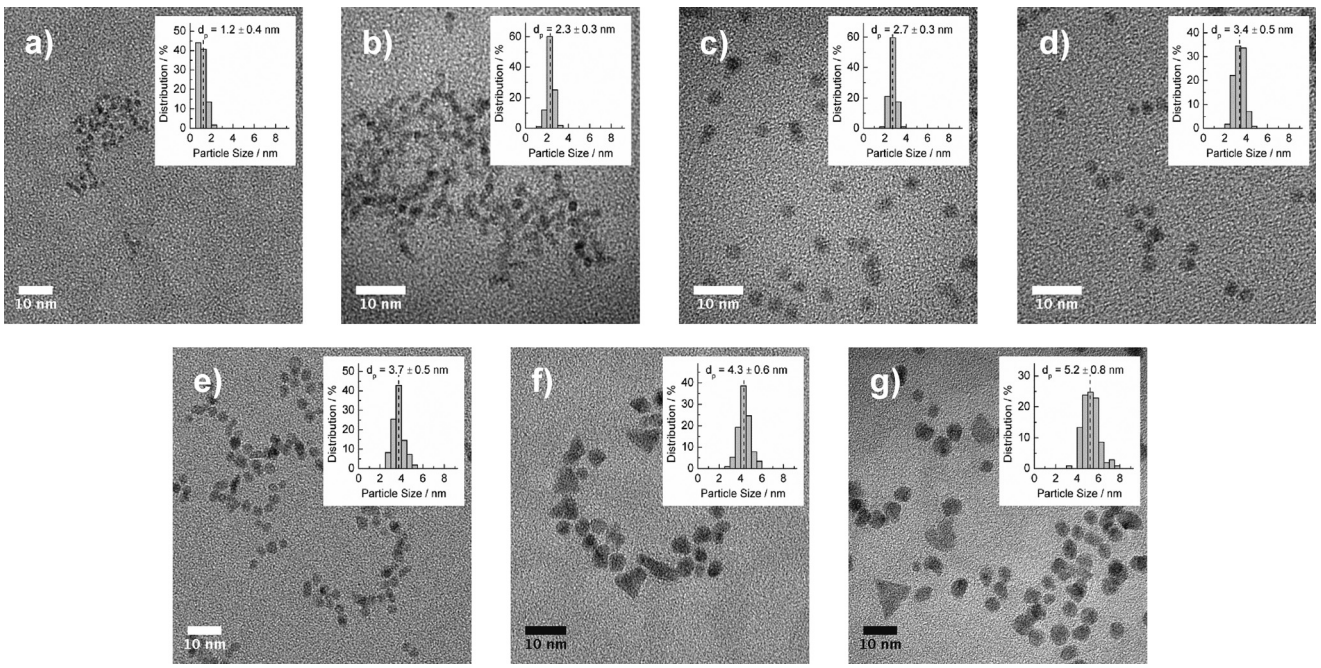

Fig. 1 Electron micrographs and particle size distributions for (a) Ru-1.2, (b) Ru-2.3, (c) Ru-2.7, (d) Ru-3.4, (e) Ru-3.7, (f) Ru-4.3, and (g) Ru-5.2.

average sizes in the range between 2.7 and 5.2 nm. Transmission electron micrographs (Fig. 1) show that Ru particles between 1.2 nm and 3.4 nm are mostly spherical. Larger particles tend to be more facetted. For the large particle size catalysts, a small fraction of tetrahedrally-shaped particles are observed, which were included in the dispersion determination.

Fig. 2a shows the Ru K-edge near-edge spectra for Ru-2.3 synthesized by polyol reduction (Ru-2.3-P) and after a second reduction with 20 bar H_2 (Ru-2.3-P-H_2). The spectra show that Ru-2.3-P and Ru-2.3-P-H_2 contain both metallic and oxidic Ru. The Ru^0 content was estimated by fitting the experimental near-edge spectra with a linear combination of reference spectra of a metallic Ru foil and RuO_2 powder. Separate X-ray Photoelectron Spectroscopy (XPS) analyses did not reveal the presence of chlorine, implying that the cationic Ru relates to small amounts of RuO_2. The Ru^0 content for Ru-2.3-P

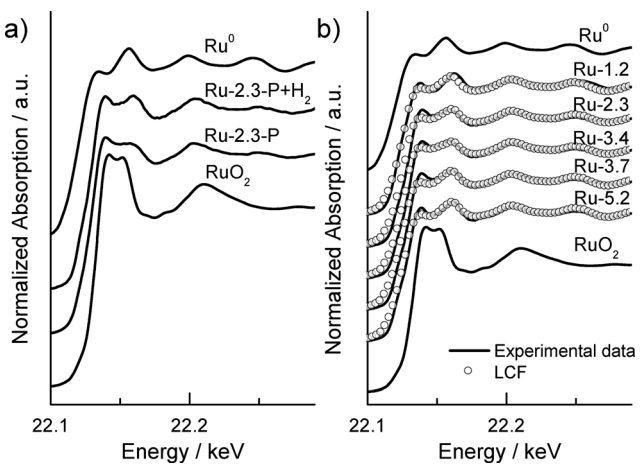

Fig. 2 Ru K-edge XANES spectra for (a) Ru-2.3 reduced in different ways and (b) Ru nanoparticles of different particle size (black lines: experimental data; circles: linear combination fitted model).

and Ru-2.3-P-H_2 were 65 and 85%, respectively. Consistent with our previous studies using $NaBH_4$ for reduction of PVP-protected nanoparticles,[27] Ru nanoparticles reduced by polyol remain partially oxidic. The reduction degree can be significantly increased by a second reduction step at 20 bar H_2 at 150 °C. The Ru K-edge near-edge spectra for differently sized Ru particles after the second reduction step (Fig. 2b) show that this difference in oxidation degree occurs for all samples. The quality of the fitting procedure is good, although one notes the small deviations in the whiteline which is expected for small nanoparticles. The estimated Ru^0 contents of the various nanoparticle catalysts are listed in Table 1. Although small metal particles seem to be more prone to oxidation than larger ones,[31] our results indicate that, after the second reduction step, the initial reduction method and particle size had only minor influence on the Ru^0 content. The average Ru^0 content was found to be 87% with a standard deviation of 5%.

Fig. 3 shows the experimental and fitted Fourier transformed k^3-weighted EXAFS and $\chi(k)\cdot k^3$ functions for four Ru nanoparticle catalysts of increasing size (fit parameters in Table 2) as well as of the Ru foil. The Fourier transforms are dominated by a Ru–Ru shell with a small contribution of a Ru–O shell. The small Ru–O contribution indicates that the Ru particles are not completely reduced in agreement with the XANES analysis. The Ru–Ru coordination number decreases when the particles become smaller. All Ru particles exhibit Ru–Ru bond lengths comparable with the bulk Ru–Ru distance (2.67 Å) with the exception of Ru-1.2 (2.64 Å).

Fig. 4 presents the FTIR spectra of four Ru nanoparticle catalysts collected at 150 °C after drying and CO adsorption. Two main features can be observed in these spectra: a strong band centered at 1990–2015 cm^{-1} region with a shoulder at 2050 cm^{-1} and a weak broad band in the 1900–1950 cm^{-1} region. The IR spectrum for Ru-1.2 shows an additional band centered around 2116 cm^{-1}. We assign these bands to the following species:[32] bridge-bonded CO at 1900 to 1950 cm^{-1}, linearly bonded CO at 1990–2015 cm^{-1}, dicarbonyl CO species adsorbed on Ru^0 at 2050 cm^{-1} and CO adsorbed on Ru^{n+} at 2116 cm^{-1}. A notable finding is that the band assigned to linearly adsorbed CO sites is red-shifted when the nanoparticle size is decreased from 4.3 to 1.2 nm. The shift is greatest when the average particle size decreases from 2.3 nm (2009 cm^{-1}) to 1.2 nm (1990 cm^{-1}). CO is still linearly bonded when the band shift from 2009 to 1990 cm^{-1}, within the range usually observed for linearly bonded CO.[32] Therefore, the shift is best explained by stronger adsorption of CO. It is also seen that a shoulder appears at 2050 cm^{-1} with decreasing particle size, which is due to Ru-dicarbonyl species. These surface complexes are likely due to CO adsorption on very low coordinated Ru surface atoms such as corner sites. The increase of this band is greatest when the particle size is decreased from 2.3 to 1.2 nm. This is consistent with the decrease in coordination number for smaller particles as determined by EXAFS. The band at 2116 cm^{-1} is due to the presence of a small amount of oxidic Ru species on Ru-1.2. It is also seen that the band due to bridge bonded CO is maximum for 3.4 nm Ru nanoparticles. The reason for this trend is unclear, but signifies the different surface structure of the nanoparticles depending on their size.

Table 2 Fit parameters of k^3-weighted EXAFS data of a Ru foil and Ru nanoparticle catalysts

	EXAFS fit parameters[a]				
Catalyst	Shell	N	R (Å)	$\Delta\sigma^2$ (Å^2)	ΔE_0 (eV)
Ru foil	Ru–Ru	12	2.68	0.004	−7.9
Ru-1.2	Ru–Ru	6.1	2.64	0.005	−6.1
Ru-2.3	Ru–O	1.4	1.99	0.002	−0.5
	Ru–Ru	6.9	2.67	0.007	
Ru-3.7	Ru–O	1.1	1.97	0.002	−3.3
	Ru–Ru	7.5	2.67	0.006	
Ru-5.2	Ru–O	1.0	1.93	0.004	−2.6
	Ru–Ru	8.7	2.67	0.007	

[a] Only first Ru–O and Ru–Ru shells fitted: Δk = 2.5–13.4 Å^{-1}; estimated errors in R: ±0.01 Å, N: ±20%, and $\Delta\sigma^2$: ±10%.

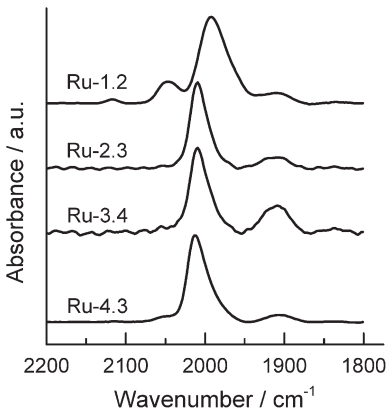

Fig. 4 CO adsorption FTIR spectra measured at 150 °C for reduced Ru nanoparticles.

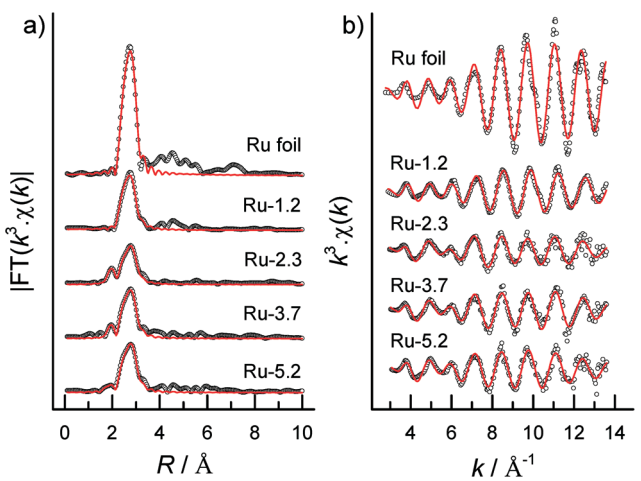

Fig. 3 Experimental (○) and fitted model (red lines) for (a) FT EXAFS functions and (b) k^3-weighted EXAFS oscillations of the Ru foil, Ru-1.2, Ru-2.3, Ru-3.7 and Ru-5.2 after polyol and H_2 reduction steps.

3.2 Catalytic activity measurements

3.2.1 Effect of temperature. Fig. 5 shows the effect of reaction temperature on the activity of aqueous phase FT synthesis for Ru-1.2 and Ru-5.2. With an increase of the reaction temperature from 130 to 230 °C, the CO consumption rate increases from 0.2 to 44.4 and from 0.2 to 12.7 mmol g_{Ru}^{-1} h^{-1} for Ru-1.2 and Ru-5.2, respectively (Fig. 5a). For these spent catalysts, TEM images shown in Fig. 6 reveal that the average size of the particles was nearly similar to that of the initial samples at 1.4 and 5.4 nm, respectively, implying that no severe sintering takes place during the FT reaction. The apparent activation energies (E_{act}^{app}) calculated from these data (Fig. 5b) are 91 (Ru-1.2) and 75 (Ru-5.2) kJ mol^{-1}. Within the carbide mechanism the activation energies relate to the apparent activation energies of the CH_x formation reaction from adsorbed CO.[33] The changes in apparent activation energies (E_{act}^{app}) with particle size are possibly due to the changes in the selectivity of oxygenates *versus* hydrocarbons to be discussed in the next section. These values for E_{act}^{app} are in the same range as values (67–109 kJ mol^{-1}) reported for the gas-phase FT reaction using Ru catalysts.[34] Fig. 7a shows the hydrocarbon and oxygenate selectivities for Ru-1.2 and Ru-5.2. Their general trend as a function of temperature is comparable to the trend earlier reported by us for 2 nm Ru nanoparticles:[27] increasing the temperature results in decrease of the oxygenate selectivity. Oxygenates are the product of termination by inserting CO into the growing chain. Simulations indicate that high CO coverage is consistent with hydrocarbon as well as oxygenate formation.[33] The temperature dependence of oxygenate selectivity can relate to either (i) different CO activation barriers of the respective sites that form oxygenates or hydrocarbons or (ii) the activation energy for termination to hydrocarbons being higher than that to oxygenates.

It has been shown before that secondary reactions of the reaction products of the FT reaction may significantly affect the product distribution.[35–37] Relevant to the present work, Chen *et al.* reported the degradation of oxygenates to hydrocarbons under a H_2 pressure of 98 bar using a Ru catalyst.[38,39] This reaction involves acid-catalyzed dehydration of alcohols and subsequent hydrogenation to paraffins.[40] The reaction mixture in the work of Chen *et al.* was slightly acidic due to the presence of organic acids.[38,39] To exclude the possibility that the selectivity changes as a function of temperature are caused by secondary reactions of aldehydes and alcohols in the present work, we carried out several additional FT reactions in the presence of decanal. Shorter chain aldehydes could not be used for this purpose because it was not possible to analyze them nor their products in our aqueous-phase FT approach. We verified that the pH of the solution was neutral before and after the reaction. Table 3 shows that the addition of decanal did not affect either the FT rate nor the selectivities and chain-growth probabilities. The main product of decanal conversion is decanol. This result shows that no preferential cracking of the oxygenated products occurs during aqueous-phase FT. It also provides a strong indication that chain-growth reactions do not proceed *via* the Pichler–Schulz mechanism. Weststrate *et al.* have recently shown that ethanol adsorbed on a Co(0001) single crystal surface can undergo C–O bond cleavage to produce

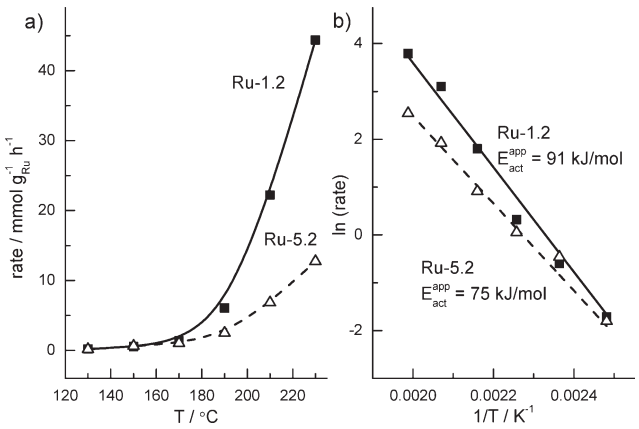

Fig. 5 Effect of reaction temperature on activity for FT reaction catalyzed by Ru-1.2 and Ru-5.2: (a) rate, and (b) Arrhenius plot.

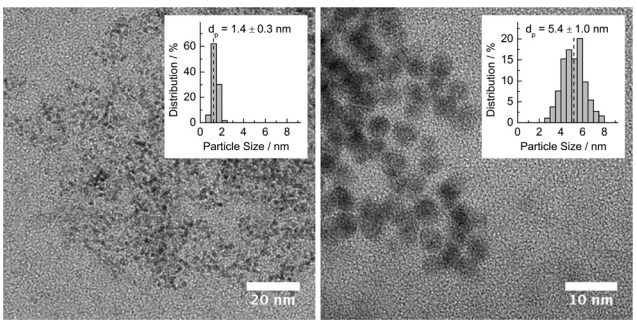

Fig. 6 Electron micrographs and particle size distributions for spent (left) Ru-1.2 and (right) Ru-5.2.

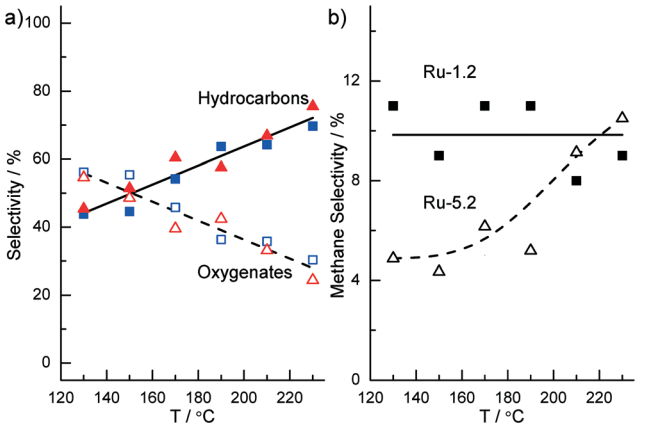

Fig. 7 Effect of reaction temperature on FT reaction catalyzed by Ru-1.2 and Ru-5.2, (a) hydrocarbons and oxygenates selectivity (hydrocarbons: ■, ▲, oxygenates: □, △, Ru-1.2: ■, □ and Ru-5.2: ▲, △), and (b) methane selectivity.

Table 3 Reactivity data for aqueous-phase Fischer–Tropsch reaction catalyzed by Ru-1.2 in the absence and presence of C10 hydrocarbon components[a]

Component	X^b (%)	FT rate (mmol g_{Ru}^{-1} h^{-1})	S_{HC} (%)	S_{OXY} (%)	α_{HC}	α_{OXY}
—	—	0.54	45	55	0.90	0.55
Decanal[c]	93	0.51	50	50	0.88	0.57
1-Decene[c]	77	0.58	50	50	0.87	0.59/0.72[d]

[a] Reaction conditions: Ru nanoparticles (50 μmol), H_2O (3 mL), P = 30 bar (H_2/CO molar ratio = 2), T = 150 °C, t = 24 h, C_{10} component (1 μmol). [b] Conversion of decanal/1-decene. [c] The contribution of decanal and 1-decene conversion was excluded from the calculation of rate, selectivity and α. [d] α_{OXY} is 0.59 from C_4 to C_{14} and changes to 0.72 above C_{14}.

C_2H_x and O surface intermediates.[41] This dissociation reaction of adsorbed ethoxy bears resemblance to the proposed C–O dissociation elementary reaction step after CO insertion during chain growth in the Pichler–Schulz mechanism. In any case, the present results show that under our reaction conditions adsorbed decanal and its hydrogenation product decanol do not undergo C–O bond cleavage to form an intermediate which can be involved in chain growth.

Another potential reaction pathway for oxygenate formation involves cationic Ru species, which are present on all of the Ru nanoparticle catalysts. We discard the possibility that cationic Ru on the nanoparticles would catalyze oxygenate formation based on a systematic previous study,[27] showing that the concentration of such cationic Ru species has no effect on the product selectivity. Related to this, we verified that oxygenates are not formed *via* the secondary hydroformylation of product olefins. This reaction is typically catalyzed by homogeneous complexes and Ru is a very active catalyst for this reaction.[42] The possibility to carry out hydroformylation with metallic nanoparticles has also been reported recently.[43] To further test the possible role of hydroformylation for oxygenates formation, we carried out an additional experiment by adding 1-decene to the reaction mixture. Table 3 shows that its addition did not significantly affect the FT rate. 1-Decene was mainly converted to *n*-decane. The selectivity of C_{11}-oxygenates was 4%, which is only marginally higher than the selectivity of 2% for the experiment without addition of 1-decene. It is interesting to observe that addition of 1-decene resulted in an increase in α_{OXY} for oxygenated products longer than C_{11}, whilst the chain-growth probability for shorter oxygenates was unaffected (Table 3 and Fig. 8). The chain-growth probability for hydrocarbons was also unaffected. This result clearly shows that 1-decene is re-adsorbed on the catalytic surface and used in further chain growth of oxygenates and not of hydrocarbons. The main conclusion from these results is that oxygenate formation does not occur *via* hydroformylation of intermediate olefins. The finding that 1-decene participates in further chain growth of oxygenates provides an additional indication that the surface intermediate for oxygenate chain growth is different from the one for hydrocarbons chain growth. This would decouple the mechanisms for formation of hydrocarbons and oxygenates. We have earlier excluded the effect of organic capping agent and solvent as the main factor in the formation of oxygenates.[29c]

Fig. 7b shows that methane selectivity for both Ru-1.2 and Ru-5.2 are below 12% in the temperature regime 130 to 230 °C. Ru-1.2 shows substantially higher methane selectivity. It is independent of temperature. For Ru-5.2, the initially lower methane selectivity increases from 5 to 10% when temperature increases. This difference in methane selectivity indicates that, for different particle sizes, there is a change in the competition for CH_x to terminate as methane *versus* being incorporated into the growing chain. The constant

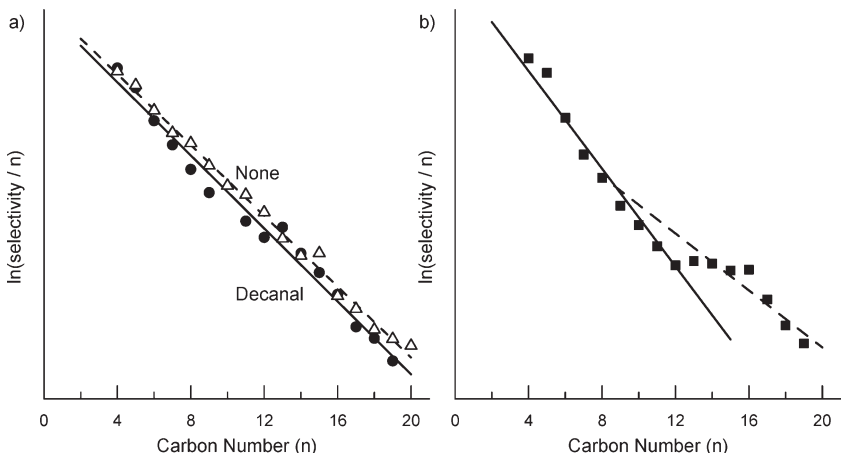

Fig. 8 Anderson–Schulz–Flory plot for oxygenates produced in FT reaction catalysed by Ru-1.2 (a) in the absence and presence of decanal, and (b) in the presence of decene.

selectivity for methane on the small particle catalyst suggests a common intermediate with the growing hydrocarbon chains. Higher methane selectivity is consistent with the activation energy of CO activation being higher than that of methane formation.[33]

The effect of temperature on the chain-growth probability for Ru-1.2 and Ru-5.2 is shown in Fig. 9. As the short-chain oxygenates could not been measured in our experiments, the chain-growth probabilities are calculated based on C_{4+} products only. It is important to note that similar to our earlier report the chain growth probabilities for hydrocarbons (α_{HC}) and oxygenates (α_{OXY}) are different.[27] This is explained in terms of different reaction centers for formation of these two product classes on the Ru nanoparticle surface.[27] Upon increasing the reaction temperature from 130 to 230 °C, the hydrocarbon chain growth probability (α_{HC}) is found to decrease for both considered nanoparticle catalysts. This behavior is typical[44,45] and consistent with the higher activation energy for chain-growth termination compared to the overall rate of chain growth.[7,8]

The chain-growth probabilities for Ru-1.2 and Ru-5.2 show anomalous temperature dependence. The initial increase of α_{OXY} for Ru-5.2 with temperature is comparable to what was found previously for 2 nm Ru nanoparticles.[27] For Ru-1.2, α_{OXY} goes through a maximum at 210 °C and decreases with further temperature increase. The increase in α_{OXY} is much more pronounced for Ru-1.2 compared to Ru-5.2. Trends for α will be further elaborated in the discussion section using kinetic considerations.

3.2.2 Effect of particle size. As apparent from several recent reports,[17–22] the FT reaction is structure sensitive for small metal nanoparticles. We investigated the effect of particle size in aqueous FT synthesis in more detail at a temperature of 150 °C. The particle size dependence of the FT activity is shown in Fig. 10. The weight-based rate of the Ru nanoparticle catalysts shows a maximum around 2.3 nm for particles between 1.2 and 3.7 nm. With a further increase of the Ru nanoparticle size the rate increases strongly. When the surface-atom normalized rates (TOF) are plotted against particle size (Fig. 10b), it is seen that the activity increases with particle size with a plateau between 2.3 and 3.7 nm. These activity trends are in very good qualitative agreement with literature data for supported Ru nanoparticle catalysts.[21,22] Both Kang *et al.*[21] and Carballo *et al.*[22] reported that the FT activity of Ru nanoparticles decreased below a critical size of 7–10 nm. Kang *et al.* investigated Ru nanoparticles sized between 3 and 10 nm supported on carbon nanotubes.[21] Carballo *et al.* studied Ru/Al_2O_3 with Ru nanoparticle sizes between 4 and 23 nm.[22] Neither literature report included Ru particles smaller than 2 nm. Similar to our observations, the surface-atom normalized TOF reported by Kang *et al.* shows a region of structure insensitivity in the FT reaction between 2.5 and 4 nm and an increase in TOF for particles larger than 4 nm. Consistent with this, Carballo *et al.* found that TOF increases for particles larger than 4 nm.[22]

Although the origin of the particle size dependence has not been elucidated yet, our data support the assumption that a minimum size of the nanoparticles is required to sustain step-edge sites needed for facile CO dissociation.[7,17] In line with the early suggestions of Van Hardeveld and Montfoort,[46] Honkala *et al.* reported that particles smaller than 2 nm do not contain step-edge sites.[47] On highly regular cuboctahedron particle highest density of step-edge sites is predicted for a particle size of about 1.5–2 nm.[47] It has been argued that in the absence of step-edge sites, CO dissociation may preferentially occur *via* H-assisted pathways.[9,10,48,49] Recent quantum-chemical calculations for Ru surfaces show that direct CO dissociation on step-edge sites is preferred over H-assisted CO dissociation.[11] In the absence of a clear method to determine the step-edge site density, we cannot

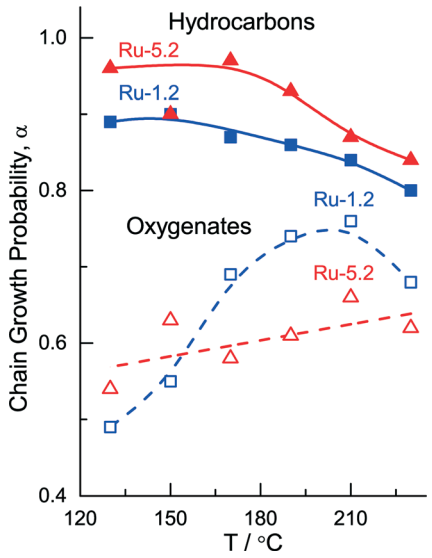

Fig. 9 Effect of reaction temperature on the chain growth probability for FT reaction catalyzed by Ru-1.2 and Ru-5.2 (hydrocarbons: ■, ▲, oxygenates: □, △, Ru-1.2: ■, □ and Ru-5.2: ▲, △).

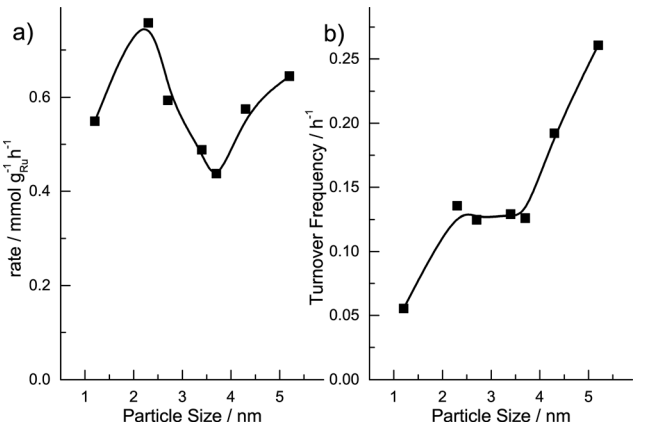

Fig. 10 Effect of particle size on the FT reaction: (a) rate and (b) surface normalized turnover frequency (TOF).

firmly conclude on the origin for the activity trends as a function of particle size. It should be noted that the Honkala data are based on idealized 'Wulff' nanoparticles. Chorkendorff's group recently employed CO isotope scrambling on differently sized Ru nanoparticles (3–12 nm) and found that the scrambling activity increases with particle size.[50] This trend was correlated to the increased density of step-edge sites for larger particles. Indeed, several further indications from literature strengthen the supposition that step-edge sites are also formed on terraces of larger nanoparticles.[51–56] For instance, Nielsen *et al.* reported that large Ru particles have a different morphology with rougher surfaces than relatively small particles.[51] In another study, Karim *et al.* found that supported Ru with larger particle size form unusual shapes.[52] By combining EXAFS structure analysis with a theoretical model, they concluded that larger particles contain more step sites. Adsorbates can also cause roughening of smooth single crystal surfaces, giving rise to the formation of defects such as step-edge sites. Surface roughening of smooth single crystal surface induced by CO and H_2 has been reported for Pt and Rh[53] as well as Co.[54–56] Hence, we speculate that the surface planes on Ru nanoparticles greater than 4 nm are large enough to accommodate further layers of Ru giving rise to increased density of step-edge sites. Although the present data clearly confirm that the performance most strongly depends on particle size and not on the Ru^0 content, it remains to be determined how the exact synthesis conditions affects the surface composition of the nanoparticles. We expect that the surface structure of nanoparticles will critically depend on the method of preparation and pretreatment.

Fig. 11a shows that the oxygenate selectivity decreases when the particle size increases from 2.3 to 5.2 nm but increases when size increases from 1.2 to 2.3 nm. The lower oxygenate selectivity for the Ru-1.2 nm compared to the 2.3 nm particles is due to the higher selectivity towards methane as shown in Fig. 12. The higher methane selectivity on the 1.2 nm is probably due the higher surface density of sites with higher barrier for CO dissociation, which favors methane formation.[7] We hypothesize that methane formation occurs on the oxygenate growth sites with high barrier for CO dissociation. With a higher concentration of sites with high barrier for CO dissociation, one would expect more methanol being formed. Oxygenates with less than four carbon atoms could not be analyzed due to experimental limitations. In order to understand the effect of higher methane selectivity, we recalculated the selectivity by taking into account only C_{4+} products (denoted as selectivity (C_{4+})). Fig. 11b shows that the selectivity (C_{4+}) for oxygenates remained constant from 1 to 3 nm and decreased with further increase in particle size. This indicates that the ratio of oxygenate to hydrocarbon formation sites remains constant when the particle size increases from 1 to 3 nm. The decrease in oxygenate selectivity (C_{4+}) above 3 nm could either imply that (i) the ratio of oxygenates to hydrocarbons growth sites decreases, or (ii) the intrinsic rate of oxygenate formation decreases with respect to hydrocarbon formation. Recent SSITKA experiments have shown that the

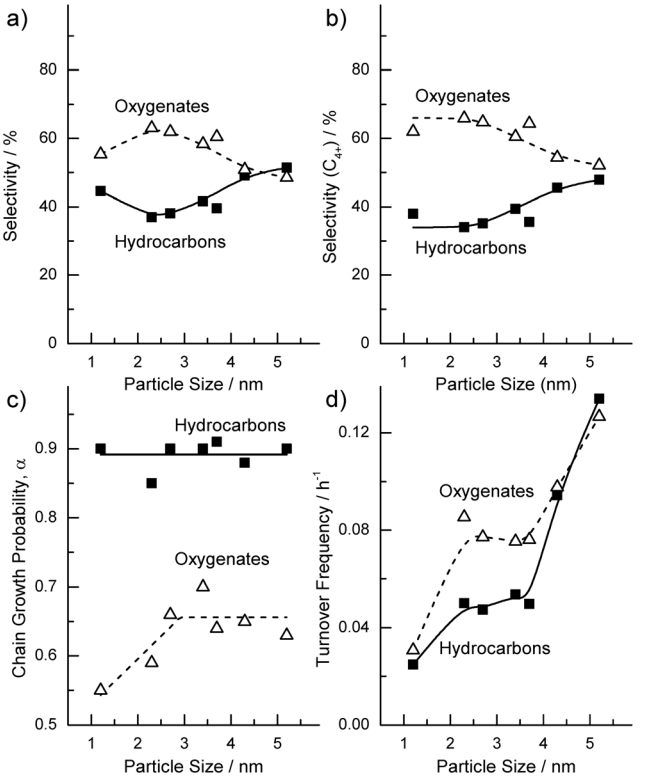

Fig. 11 Effect of particle size on the FT reaction: (a) selectivity, (b) selectivity for C_{4+} products, (c) hydrocarbons and oxygenates chain growth probability, and (d) activities for hydrocarbons and oxygenates formation.

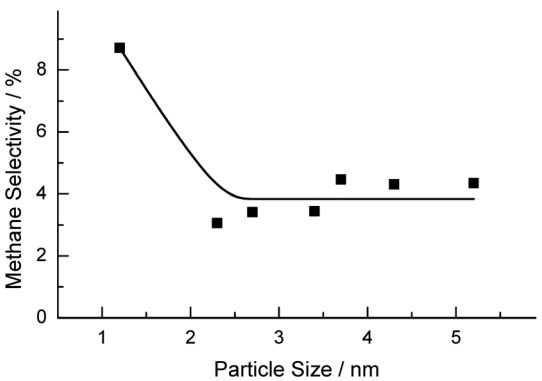

Fig. 12 Effect of particle size on methane selectivity in FT reaction.

residence time for CH_x species is independent of Ru particle size.[22] If CH_x residence time remains unchanged, we would expect that the change in the intrinsic rate of oxygenate or hydrocarbon formation affects α. However, as Fig. 11c shows that, above 3 nm, both α_{OXY} and α_{HC} are not influenced by the increase in Ru particle size, we conclude that there is no change in the intrinsic rate of oxygenate or hydrocarbon formation. Hence, the decrease in the selectivity (C_{4+}) for oxygenates with particle size is primarily due to the decrease in the relative ratio of oxygenates to hydrocarbons growth sites.

Fig. 11c shows that α_{HC} is independent of particle size, while α_{OXY} increases from 1 to 3 nm but remains constant above 3 nm. Hydrocarbons are shown to exhibit higher chain-growth probability compared to oxygenates. This supports our earlier proposal that oxygenates and hydrocarbons are formed on two different catalytic centers.[27] If oxygenates and hydrocarbons would be formed on similar catalytic site with only a different termination step, one would expect trends in α with Ru particle size to be the same for oxygenates and hydrocarbons. In addition, the lower α_{OXY} compared to α_{HC} is consistent with CO dissociation at oxygenates growth sites having a higher activation barrier, and the termination step to oxygenates having a lower activation barrier compared hydrocarbons as follows from eqn (8) in the discussion section.

The surface-atom normalized rates for hydrocarbon (TOF_{HC}) and oxygenate (TOF_{OXY}) formation as a function of the particle size are given in Fig. 11d. It can be seen that both rates increase with the particle size. The increase of TOF_{HC} with particle size is consistent with the proposed increasing density of step-edge sites. Fig. 11c shows that, despite the increasing density of these sites for facile CO dissociation, the chain-growth probability for hydrocarbons remains constant. A rationalization for this behavior is that each site for CO dissociation is kinetically coupled to a chain growth site. Such a dual reaction center model has been first proposed by Shetty *et al.*[57] and its kinetic implications have been recently developed.[6] This insensitivity of reactivity of the reaction centers to particle size is in line with SSITKA experiments in which the residence time of CH_x species on the surface of a Ru catalyst was found to be independent of particle size.[22] Note that these latter measurements were carried out at temperatures where hydrocarbon formation is dominant. Since chain growth is predicted to be structure insensitive,[58] a constant residence time for CH_x intermediates will lead to similar chain length and, hence constant, α_{HC}. Previous studies have also shown that α_{HC} is independent of particle size for supported Ru and Co catalysts.[44,45]

The kinetic observations for oxygenate formation are quite different from those for hydrocarbon formation. Two regions can be discerned. One with Ru nanoparticles in the range from 1 to 3 nm, and a second with Ru particles ranging from 3 to 5 nm. When the particle size is increased from 3 to 5 nm, TOF_{OXY} increases and α_{OXY} remains constant. This implies that more dissociated CO is converted into oxygenates, while the chain length remains constant. This can be explained by an increase in the number of oxygenate growth sites. Similar to the hydrocarbon growth sites, each site for CO dissociation is coupled to an oxygenate growth sites for Ru particles larger than 3 nm. Since we have hypothesized that oxygenates are formed on planar sites with higher barrier for CO dissociation,[27] the increase in TOF_{OXY} for Ru larger than 3 nm can be explained by the Ru particles having larger planar facets which can accommodate more oxygenates growth sites. In contrast, increasing the Ru particle size from 1 to 3 nm (the first range) results in an increasing TOF_{OXY} in parallel with an increasing α_{OXY}. This means that more and longer oxygenate chains are formed. This trend cannot be explained by an increase in the number of oxygenates growth sites only. If one also considers the trend for methane selectivity (Fig. 12), the increase in α_{OXY} (Fig. 11c) is complemented by a decrease in the methane selectivity when the Ru particles size increases from 1 to 3 nm. We have earlier proposed that the oxygenate formation sites are also favorable for methane formation due to the higher barrier for CO dissociation. The decrease in methane selectivity will lead to higher CH_x coverage near the oxygenates growth site and, accordingly, more CH_x species are available for oxygenate chain growth. Consequently, this leads to higher chain growth rate at the oxygenates growth sites and α_{OXY} increases.

4. Discussion

4.1 Effect of temperature on FT reaction

The anomalous trend of increasing α for oxygenate formation with temperature (Fig. 9) is a consequence of the decreasing apparent activation barrier for CO dissociation.[7,8] It results in an increase of the apparent activation energy of chain growth *versus* the rate of chain termination. This can be deduced in the following way. The chain-growth probability can be expressed as

$$\alpha(C_i) = \frac{r_{prop}(C_i)}{r_{prop}(C_i) + r_{term}(C_i)}; i \geq 1 \quad (5)$$

where $r_{prop}(C_i)$ is the rate of propagation of a carbon chain C_i with length i to a carbon chain C_{i+1} with length $i + 1$ and $r_{term}(C_i)$ the rate of termination of a carbon chain with length i. An expression for the steady-state coverage of the building blocks, which are CH_x surface species in the carbide mechanism, θ_{CH_x}, is

$$\frac{d\theta_{CH_x}}{dt} = r_{CO\,diss} - r_{methane} - \sum_{i=1}^{\infty} r_{prop}(C_i) \quad (6)$$

in which the terms on the right hand side reflect the rates of CO dissociation, methanation (CH_x hydrogenation) and propagation by C–C coupling of CH_x to all growing hydrocarbon chains C_i forming C_{i+1}, respectively. One deduces from eqn (6) that in order to generate a high surface coverage of CH_x, the rate of CO dissociation has to be high and the rate of methane formation low. Assuming that (i) the rate of water formation is fast, and (ii) the rate of propagation is much faster than CH_x formation and the rate of termination, the following expression for α can be derived.[28]

$$\alpha = \left(1 + \left(\frac{k_{term}^{\,2}}{k_{prop} \cdot k_{CO\,diss} \cdot \theta_{CO} \cdot (1 - \theta_{CO})}\right)^{\frac{1}{3}}\right)^{-1} \quad (7)$$

According to the carbide mechanism, the formation of oxygenates occurs *via* CO insertion into the growing chain as

a terminating step. We modify eqn (7) to describe the chain-growth probability for oxygenates by replacing k_{term} with $k_{term\ oxy}\cdot\theta_{CO}$. Then, the following equation can be derived:

$$\alpha_{OXY} = \left(1+\left(\frac{k_{term\ oxy}{}^{2}\cdot\theta_{CO}}{k_{prop}\cdot k_{CO\ diss}\cdot(1-\theta_{CO})}\right)^{\frac{1}{3}}\right)^{-1} \quad (8)$$

The change in α_{OXY} with temperature was then modeled using eqn (8) and the values used in the Arrhenius equation are given in Table 4. The surface CO coverage was estimated by a simple method using the Van't Hoff equation and assuming θ_{CO} to be 0.8 at 130 °C with E^{ads}_{CO} of 130 kJ mol^{-1}. Fig. 13 shows that α_{OXY} increases with temperature under our specified conditions, which supports the experimental findings in Fig. 9. $E^{ads}_{CO\ diss}$, E^{ads}_{prop} and E^{ads}_{term} are shown to significantly affect α_{OXY}. An increase in $E^{ads}_{CO\ diss}$ and/or E^{ads}_{prop} would decrease α_{OXY}, while an increase in E^{ads}_{term} would increase α_{OXY}. Fig. 13a shows that when $E^{ads}_{CO\ diss} < E^{ads}_{prop} < E^{ads}_{term}$, the rate of CO dissociation is very fast and termination occurs very slowly. Hence, α_{OXY} approaches 1. Furthermore, when the rate of CO dissociation is high, the surface coverage of CO will be low and the probability to terminate by CO insertion is low. In contrast, for $E^{ads}_{prop} > E^{ads}_{term} \gg E^{ads}_{CO\ diss}$, there is insufficient CH_x for chain growth so that termination is slow and, henceforth, α_{OXY} approaches 0. This implies that only methane and methanol will be formed. Based on this analysis, for the formation of long chain oxygenates $E^{ads}_{CO\ diss}$ should not be too low to maintain sufficient CO on the surface near the oxygenate growth site for termination by CO insertion. High $E^{ads}_{CO\ diss}$ has to be accompanied by low E^{ads}_{prop} and high E^{ads}_{term} to allow chain growth.

Table 4 Kinetic parameters used in simplified model to predict chain growth probabilities for oxygenates (OXY) and hydrocarbons (HC)

Rate constant	A_o (s^{-1})	E_{act} (kJ mol^{-1})
$k_{CO\ diss\ OXY}$	10^{13}	110
$k_{prop\ OXY}$	10^{13}	60
$k_{term\ OXY}$	10^{17}	80
$k_{CO\ diss\ HC}$	10^{13}	50
$k_{prop\ HC}$	10^{13}	60
$k_{term\ HC}$	10^{17}	80

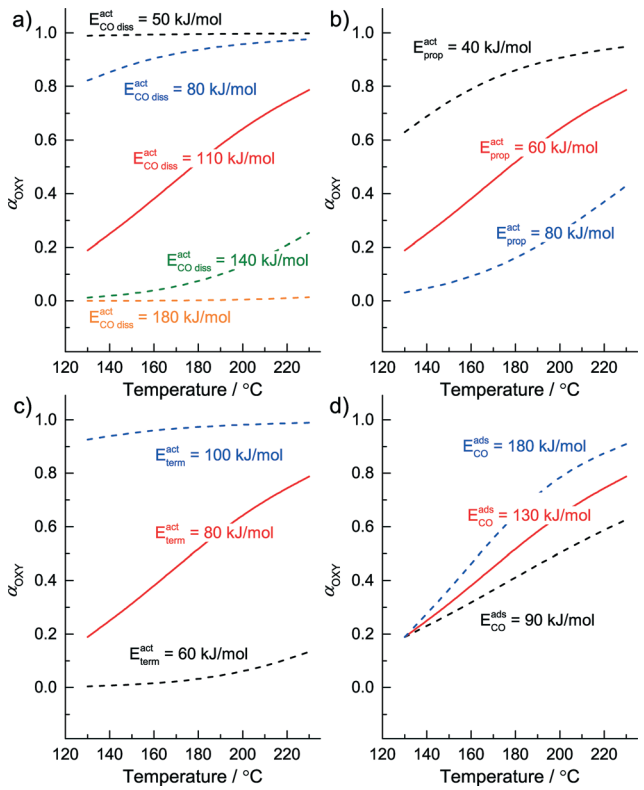

Fig. 13 Simplified kinetics model for oxygenates chain growth probability with varying activation energy for (a) CO dissociation, (b) propagation, (c) termination, and (d) CO adsorption energy.

The change in α_{HC} is modeled using eqn (7). For easier comparison, the values used to model α_{OXY} in Table 4 will be used, except that a value of $E^{ads}_{CO\ diss}$ of 50 kJ mol^{-1} was used for the base case, the low value being consistent with the proposal that hydrocarbons are formed on sites with relatively low barrier for CO dissociation. From Fig. 14, the conventional temperature dependence of decreasing α with temperature is always observed. This is in agreement with our results for α_{HC} in Fig. 9 and also those reported in literature.[44,45] Similar to the findings for α_{OXY}, an increase in $E^{ads}_{CO\ diss}$ and/or E^{ads}_{prop} would lead to a decrease in α_{HC}, and an increase in E^{act}_{term} would increase α_{HC}. Hence, to maintain high chain growth for hydrocarbon, $E^{ads}_{CO\ diss}$ and E^{ads}_{prop} should be as low as possible and E^{ads}_{term} should be high.

Fig. 13d and 14d show that the change in E^{ads}_{CO} affects α_{OXY} and α_{HC} very differently. Higher E^{ads}_{CO} leads to higher α_{OXY} but lower α_{HC}. However, consistent to both α_{OXY} and α_{HC}, higher E^{ads}_{CO} leads to more rapid changes in α. This relates to the dependence of the overall rate of CO dissociation on the desorption barrier of CO as observed from eqn (9).

$$E^{act}_{app,CO\ diss} = E^{act}_{CO\ diss} - (1-2\theta_{CO})\cdot E^{ads}_{CO} \quad (9)$$

On the oxygenate formation sites, the activation barrier for CO dissociation is high and θ_{CO} is also high. This means that in order for CO dissociation to occur a vacancy needs to be available requiring CO desorption. This will lead to $E^{act}_{app,CO\ diss} > E^{act}_{CO\ diss}$ when θ_{CO} approaches 1. Hence, the higher CO adsorption energy will lead to higher $E^{act}_{app,CO\ diss}$, and the rate of CO dissociation will increase more rapidly with temperature resulting in higher α_{OXY}. In contrast, on the hydrocarbon growth site where barrier for CO dissociation is low and θ_{CO} is low, the adsorption of CO will lower $E^{act}_{app,CO\ diss}$. Accordingly, $E^{act}_{app,CO\ diss} > E^{act}_{CO\ diss}$ when θ_{CO} approaches 0. Also, higher CO adsorption energy will lead to lower $E^{act}_{app,CO\ diss}$, and the rate for CO dissociation will increase much slower compared the rate of termination with temperature, resulting in lower α_{HC}.

The anomalous temperature dependence of α_{OXY} is inconsistent with the alternative Pichler–Schulz CO insertion

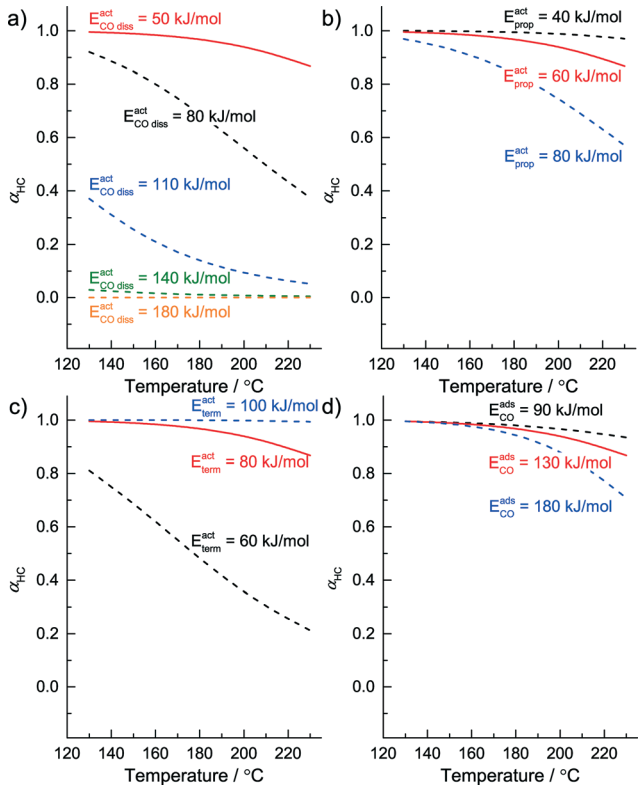

Fig. 14 Simplified kinetics model for hydrocarbons chain growth probability with varying activation energy for (a) CO dissociation, (b) propagation, (c) termination, and (d) CO adsorption energy.

mechanism for chain growth. The expression for α according to the Pichler–Schulz mechanism is

$$\alpha_{PS} = \frac{k_{prop} \cdot \theta_{CO}}{k_{prop} \cdot \theta_{CO} + k_{term}} \quad (10)$$

In contrast to expression (7), k_{term} will always have a higher activation energy for high α.

From the methane selectivity (Fig. 7b) and α_{OXY} (Fig. 9), Ru-1.2 and Ru-5.2 are shown to exhibit very different trends. This indicates that the chemical nature of the reactive sites are different for these two catalysts. From the trends in Fig. 7b and 9, two important observations are made, namely (i) constant methane selectivity for Ru-1.2 is accompanied by a steep increase in α_{OXY}, and (ii) increasing methane selectivity for Ru-5.2 is accompanied by gradual increase in α_{OXY}. These trends can be explained based on eqn (6) to (8). Increasing methane selectivity with temperature for Ru-5.2 indicates methane formation has a higher barrier than for Ru-1.2, which becomes more important at high temperature for Ru-5.2. Based on eqn (6), the consumption of CH_x for methanation would result in less CH_x available for the C–C coupling chain growth step. Hence, when more CO dissociates for Ru-5.2 with increasing temperature, there would be an increase in competition for CH_x species between methanation and oxygenates chain growth. In comparison, for Ru-1.2, constant methane selectivity indicates that the relative rate of methanation remains unchanged. When more CH_x species are being formed, they are predominately being utilized for chain growth. Consequently, this leads to a more pronounced increase in α_{OXY} for Ru-1.2 compared to Ru-5.2. These results also imply that methane formation for Ru-1.2 is due the low rate of CO dissociation, but for Ru-5.2 methane formation is controlled by the activation energy for methanation. Another contributing factor to the faster increase in α_{OXY} could be the strength of CO adsorption. As observed from CO ATR-IR studies and the dependence of the surface coordination number on Ru nanoparticle size as determined from EXAFS, smaller particles will bind CO more strongly than the larger particles. As discussed earlier and also shown Fig. 13d, higher E^{ads}_{CO} would increase α_{OXY} more rapidly.

5. Conclusions

We have shown that in aqueous-phase FT the chain growth probabilities of oxygenates and hydrocarbons exhibit different trends with respect to temperature and particle size. This indicates that two different sites are responsible for their formation. With increasing temperature, α_{HC} decreases as usually observed in conventional FT synthesis. Conversely, increasing temperature leads to an increase in α_{OXY}. We propose that the increase in α_{OXY} is caused by the high apparent activation energy of CO dissociation, which is due to a high CO coverage. This essentially hinders CO dissociation, since the rate of chain termination by CO insertion is relatively fast. Results were analyzed with a kinetic model and are consistent with the carbide mechanism. The increasing α_{OXY} and decreasing oxygenate selectivity with temperature cannot be explained using the Pichler–Schulz mechanism. An increase in Ru particle size leads to a decrease in the oxygenate selectivity, indicating that the relative ratio of oxygenates to hydrocarbons growth sites decreases. The kinetic parameters point to an increasing density of active sites for hydrocarbons and oxygenates formation with increasing particle size. The relative ratio of oxygenates to hydrocarbons growth sites becomes smaller for larger particles.

Acknowledgements

The authors thank the National Research School Combination on Catalysis for financial support, NWO-Dubble for access to X-ray absorption spectroscopy facilities at ESRF, ESRF staff for their support and the Soft Matter Cryo-TEM Research Unit for access to the TEM facility. We thank Adelheid Elemans for the elemental analysis, Dr. Peter Thüne and Ajin Cheruvathur for providing assistance with ATR-IR measurements.

References

1 J. J. Spivey and A. Egbebi, *Chem. Soc. Rev.*, 2007, **36**, 1514–1528.

2 E. van Steen and M. Claeys, *Chem. Eng. Technol.*, 2008, **31**, 655–666.
3 A. Y. Khodakov, W. Chu and P. Fongarland, *Chem. Rev.*, 2007, **107**, 1692–1744.
4 Q. Zhang, J. Kang and Y. Wang, *ChemCatChem*, 2010, **2**, 1030.
5 B. H. Davis, *Ind. Eng. Chem. Res.*, 2007, **46**, 8938–8945.
6 A. J. Markvoort, R. A. van Santen, P. A. J. Hilbers and E. J. M. Hensen, *Angew. Chem., Int. Ed.*, 2012, **51**, 9015–9019.
7 R. A. van Santen, I. M. Ciobica, E. van Steen and M. M. Ghouri, *Adv. Catal.*, 2011, **54**, 127–187.
8 R. A. van Santen, M. M. Ghouri, S. Shetty and E. J. M. Hensen, *Catal. Sci. Technol.*, 2011, **1**, 891–911; R. A. van Santen, M. Ghouri and E. J. M. Hensen, *Phys. Chem. Chem. Phys.*, 2014, **16**, 10041.
9 I. M. Ciobica and R. A. van Santen, *J. Phys. Chem. B*, 2003, **107**, 3808–3812.
10 M. Ojeda, R. Nabar, A. U. Nilekar, A. Ishikawa, M. Mavrikakis and E. Iglesia, *J. Catal.*, 2010, **272**, 287–297.
11 S. Shetty, A. P. J. Jansen and R. A. van Santen, *J. Am. Chem. Soc.*, 2009, **131**, 12874–12875.
12 R. C. Brady and R. Pettit, *J. Am. Chem. Soc.*, 1981, **103**, 1287–1289.
13 J. Gaube and H. F. Klein, *J. Mol. Catal. A: Chem.*, 2008, **283**, 60–68.
14 H. Pichler and H. Schulz, *Chem. Ing. Tech.*, 1970, **42**, 1162–1174.
15 B. H. Davis, *Catal. Today*, 2009, **141**, 25–33.
16 E. Iglesia, S. L. Soled and R. A. Fiato, *J. Catal.*, 1992, **137**, 212–224.
17 G. L. Bezemer, J. H. Bitter, H. Kuipers, H. Oosterbeek, J. E. Holewijn, X. D. Xu, F. Kapteijn, A. J. van Dillen and K. P. de Jong, *J. Am. Chem. Soc.*, 2006, **128**, 3956–3964.
18 O. Borg, P. D. C. Dietzel, A. I. Spjelkavik, E. Z. Tveten, J. C. Walmsley, S. Diplas, S. Eri, A. Holmen and E. Ryttera, *J. Catal.*, 2008, **259**, 161–164.
19 G. Prieto, A. Martínez, P. Concepción and R. Moreno-Tost, *J. Catal.*, 2009, **266**, 129–144.
20 J. P. den Breejen, P. B. Radstake, G. L. Bezemer, J. H. Bitter, V. Froseth, A. Holmen and K. P. de Jong, *J. Am. Chem. Soc.*, 2009, **131**, 7197–7203.
21 J. Kang, S. Zhang, Q. Zhang and Y. Wang, *Angew. Chem., Int. Ed.*, 2009, **48**, 2565–2568.
22 J. M. G. Carballo, J. Yang, A. Holmen, S. Garcia-Rodriguez, S. Rojas, M. Ojeda and J. L. G. Fierro, *J. Catal.*, 2011, **284**, 102–108.
23 A. Tuxen, S. Carenco, M. Chintapalli, C.-H. Chuang, C. Escudero, E. Pach, P. Jiang, F. Borondics, B. J. Beberwyck, A. P. Alivisatos, G. Thornton, W.-F. Pong, J. Guo, R. Perez, F. Besenbacher and M. Salmeron, *J. Am. Chem. Soc.*, 2013, **135**, 2273–2278.
24 D. I. Enache, B. Rebours, M. Roy-Auberger and R. Revel, *J. Catal.*, 2002, **205**, 346–353.
25 H. L. Karaca, O. V. Safonova, S. P. Chambrey, P. Fongarland, P. Roussel, A. Griboval-Constant, M. Lacroix and A. Y. Khodakov, *J. Catal.*, 2011, **277**, 14–26.
26 (*a*) C. X. Xiao, Z. P. Cai, T. Wang, Y. Kou and N. Yan, *Angew. Chem., Int. Ed.*, 2008, **47**, 746–749; (*b*) L. Liu, G. Sun, C. Wang, J. Yang, C. Xiao, H. Wang, D. Ma and Y. Kou, *Catal. Today*, 2012, **183**, 136; (*c*) H. Wang, W. Zhou, J.-X. Liu, R. Si, G. Sun, M.-Q. Zhong, H.-Y. Su, H.-B. Zhao, J. A. Rodriguez, S. J. Pennycook, J.-C. Idrobo, W.-X. Li, Y. Kou and D. Ma, *J. Am. Chem. Soc.*, 2013, **135**, 4149.
27 X. Y. Quek, Y. Guan, R. A. van Santen and E. J. M. Hensen, *ChemCatChem*, 2011, **3**, 1735–1738.
28 C. Wang, H. Zhao, H. Wang, L. Liu, C. Xiao and D. Ma, *Catal. Today*, 2012, **183**, 143–153.
29 (*a*) X.-Y. Quek, I. A. W. Filot, R. Pestman, R. A. van Santen, V. Petkov and E. J. M. Hensen, *Chem. Commun.*, 2014, **50**, 6005–6008; (*b*) X.-Y. Quek, Y. Guan and E. J. M. Hensen, *Catal. Today*, 2012, **183**, 72–78; (*c*) X.-Y. Quek, R. Pestman, R. A. van Santen and E. J. M. Hensen, *ChemCatChem.*, 2013, **5**, 3148–3155.
30 J. J. F. Scholten, A. P. Pijpers and A. M. L. Hustings, *Catal. Rev.: Sci. Eng.*, 1985, **27**, 151–206.
31 D. A. J. M. Ligthart, R. A. van Santen and E. J. M. Hensen, *Angew. Chem., Int. Ed.*, 2011, **50**, 5306–5310.
32 S. Y. Chin, C. T. Williams and M. D. Amiridis, *J. Phys. Chem. B*, 2006, **110**, 871–882.
33 R. A. van Santen and A. Markvoort, *ChemCatChem*, 2013, **5**, 3384–3397.
34 Y.-W. Chen and J. Goodwin Jr., *React. Kinet. Catal. Lett.*, 1984, **26**, 453–459.
35 E. Iglesia, S. C. Reyes and R. J. Madon, *J. Catal.*, 1991, **129**, 238–256.
36 R. J. Madon, S. C. Reyes and E. Iglesia, *J. Phys. Chem.*, 1991, **95**, 7795–7804.
37 J. G. Ekerdt and A. T. Bell, *J. Catal.*, 1980, **62**, 19–25.
38 L. Chen, Y. Zhu, H. Zheng, C. Zhang and Y. Li, *J. Chem. Technol. Biotechnol.*, 2012, **87**, 1089–1097.
39 L. Chen, Y. Zhu, H. Zheng, C. Zhang, B. Zhang and Y. Li, *J. Chem. Technol. Biotechnol.*, 2012, **87**, 112–122.
40 X. Y. Quek, Y. Guan, R. van Santen and E. J. M. Hensen, *ChemSusChem*, 2010, **3**, 1264–1267.
41 C. J. Weststrate, H. J. Gericke, M. W. G. M. Verhoeven, I. M. Ciobîcă, A. M. Saib and J. W. Niemantsverdriet, *J. Phys. Chem. Lett.*, 2010, **1**, 1767–1770.
42 R. Franke, D. Selent and A. Börner, *Chem. Rev.*, 2012, **112**, 5675–5732.
43 A. J. Bruss, M. A. Gelesky, G. Machado and J. Dupont, *J. Mol. Catal. A: Chem.*, 2006, **252**, 212–218.
44 G. P. Van der Laan and A. Beenackers, *Catal. Rev.: Sci. Eng.*, 1999, **41**, 255–318.
45 R. A. Dictor and A. T. Bell, *J. Catal.*, 1986, **97**, 121–136.
46 R. van Hardeveld and A. van Montfoort, *Surf. Sci.*, 1966, **4**, 396–430.
47 K. Honkala, A. Hellman, I. N. Remediakis, A. Logadottir, A. Carlsson, S. Dahl, C. H. Christensen and J. K. Norskov, *Science*, 2005, **307**, 555–558.
48 M. P. Andersson, E. Abild-Pedersen, I. N. Remediakis, T. Bligaard, G. Jones, J. Engbwk, O. Lytken, S. Horch, J. H. Nielsen, J. Sehested, J. R. Rostrup-Nielsen, J. K. Norskov and I. Chorkendorff, *J. Catal.*, 2008, **255**, 6–19.

49 G. A. Morgan, D. C. Sorescu, T. Zubkov and J. T. Yates, *J. Phys. Chem. B*, 2004, **108**, 3614–3624.
50 C. Strebel, S. Murphy, R. M. Nielsen, J. H. Nielsen and I. Chorkendorff, *Phys. Chem. Chem. Phys.*, 2012, **14**, 8005–8012.
51 R. M. Nielsen, S. Murphy, C. Strebel, M. Johansson, I. Chorkendorff and J. H. Nielsen, *J. Nanopart. Res.*, 2010, **12**, 1249–1262.
52 A. M. Karim, V. Prasad, G. Mpourmpakis, W. W. Lonergan, A. I. Frenkel, J. G. Chen and D. G. Vlachos, *J. Am. Chem. Soc.*, 2009, **131**, 12230–12239.
53 G. A. Somorjai, K. S. Hwang and J. S. Parker, *Top. Catal.*, 2003, **26**, 87–99.
54 J. J. C. Geerlings, J. H. Wilson, G. J. Kramer, H. Kuipers, A. Hoek and H. M. Huisman, *Appl. Catal., A*, 1999, **186**, 27–40.
55 J. Wilson and C. Degroot, *J. Phys. Chem.*, 1995, **99**, 7860–7866.
56 G. A. Beitel, C. P. M. de Groot, H. Oosterbeek and J. H. Wilson, *J. Phys. Chem. B*, 1997, **101**, 4035–4043.
57 S. G. Shetty, I. M. Ciobica, E. J. M. Hensen and R. A. van Santen, *Chem. Commun.*, 2011, **47**, 9822–9824.
58 R. A. van Santen, *Acc. Chem. Res.*, 2009, **42**, 57–66.